Full length article

Energetically favorable dislocation/nanobubble bypass mechanism in irradiation conditions

Wu-Rong Jian [a],*, Shuozhi Xu [a], Yanqing Su [b], Irene J. Beyerlein [a,c,1]

[a] *Department of Mechanical Engineering, University of California, Santa Barbara, Santa Barbara, California 93106-5070, USA*
[b] *Department of Mechanical and Aerospace Engineering, Utah State University, Logan UT 84322-4130, USA*
[c] *Materials Department, University of California, Santa Barbara, Santa Barbara, California 93106-5050, USA*

ARTICLE INFO

ABSTRACT

With exposure to high-energy particle irradiation, structural metals develop a number of nanoscale defects, one of which is the nano-sized He bubble. Formed throughout the material, these bubbles can directly impair the movement of dislocations and dramatically alter mechanical performance. Propagating edge dislocations in face-centered cubic metals, driven under sufficient mechanical forces, are expected to cut through He bubbles, due to the higher energetic expense. Here, using atomistic simulations for a model Cu material, we find that when the He-vacancy ratio and bubble diameter become sufficiently large and the ratio of the bubble spacing to the diameter is reduced below a threshold, an extended edge dislocation engages in a multi-step-bypass (MSB) maneuver to change its glide plane and overcome the bubble at room temperature. This unanticipated MSB mechanism provides a more energetically favorable pathway compared to conventional bypass mechanisms under these severe conditions.

© 2022 Acta Materialia Inc. Published by Elsevier Ltd. All rights reserved.

1. Introduction

Deployed in nuclear fusion and fission reactors, the metallic materials suffer from a harsh irradiation environment that involves high-energy neutron bombardment and nuclear reactions [1]. Such reactions generate large amounts of helium (He), which usually develop into He bubbles due to low solubility in metals at room temperature [2]. The appearance of He bubbles results in swelling [3], surface blistering [4], strain hardening [5–7], and macroscopic embrittlement [8]. Among them, strain hardening stems from the impediment posed by He bubbles to dislocation motion [2,5,9], and substantially alters the mechanical properties of metals over time. Understanding these microscopic interactions is imperative towards designing the next generation of irradiation-resistant materials to sustain long service lives of nuclear energy systems.

In the laboratory, direct He implantation has been applied widely to investigate the strengthening or hardening effect of He bubbles in face-centered cubic (FCC) [6,7,9–11] and body-centered cubic (BCC) [12] metals. From analyses of transmission electron microscopy images of dislocation-bubble interactions, it is possible to observe where the dislocations are located before they contact the He bubbles, when they are stopped by the He bubbles, or after they bypass He bubbles [13,14]. However, it is still challenging to identify the mechanism the dislocation uses to bypass and the energies required to do so.

In light of this, molecular dynamics (MD) simulations have been utilized widely to study the interactions between a single edge dislocation and a void [15–25] or He bubble [9,26–32]. In simulation for dislocation-void interaction, two types of bypass mechanisms have been observed, either void cutting by the dislocation [15,16,20,22] or climb of the dislocation to another parallel plane lying either above or below the equatorial plane of the void [17–19,23,33]. Dislocation climb requires vacancy diffusion to or from the dislocation core, and therefore, is promoted at elevated temperatures [34]. In BCC metals, in which the dislocation core tends to be compact, climb is the main bypass mechanism [17,18,23,33], which is a single-step process, and can occur even at room temperature [17,18,33]. Void cutting only exists in a few cases with small voids whose diameters are not larger than 1.2 nm [19]. In FCC metals, however, in which the dislocation cores in equilibrium tend to be extended, climb requires the dislocation core to first constrict to a metastable state before climbing to another parallel glide plane [35]. As the first constriction step and the subsequent formation of jogs in the dislocation can be energetically unfavorable, particularly when the intrinsic stacking fault energy (ISFE) for the FCC metal is low (≈ 40 mJ/m^2 or less), void cutting is often favored over climb

---

* Corresponding author.

E-mail address: wurong@ucsb.edu (W.-R. Jian).

[1] Irene J. Beyerlein was an Editor of the journal during the review period of the article. To avoid a conflict of interest, Irene J. Beyerlein was blinded to the record and another editor processed this manuscript.

at room temperature [15,20]. Even when, in the MD model, the ISFE in FCC Cu is artificially increased by five times to 186.5 mJ/m^2 [36], dislocation climb still only becomes favorable over dislocation cutting of the void at a high temperature of 700 K.

Most studies of dislocation-He bubble interactions focus on BCC Fe [26–32], in which dislocation climb is the only bypass maneuver that requires a lower or higher critical bypass stress than that of dislocation-void interaction [26,29,31], depending on the temperature and the ratio of He atoms to vacancies (He/V ratio) in the bubble. Especially when the He/V ratio in the bubble is high (2 or greater) at 300 K [31], the critical bypass stress reduces to 1/2–2/3 of that for voids or low He/V ratio bubbles (smaller than 1). An edge dislocation interacting with a He bubble in BCC metals gives rise to dislocation climb, creating a pair of unit jogs or superjogs. Generally, large bubble size or high He/V ratio leads to a superjog pair. The superjogged dislocation line involves greater distances climbed than a unit jog, enabling it to cut through the periphery of the bubble rather than its equatorial plane.

The interaction mechanism between edge dislocations and He bubbles in FCC metals has received far less attention. Unlike dislocations in BCC metals, edge dislocations in FCC metals dissociate into two partial dislocations separated by a stacking fault (SF) [34]. To date, only Ding et al. [9] performed MD simulations on dislocation-bubble interaction in FCC Cu at 300 K and concluded that edge dislocation cuts through He bubble and does not climb, which is similar to its response with a void [15,20]. Questions regarding the effect of bubble pressure on the interaction between a dislocation and a He bubble still remain for FCC metals. The He/V ratio in the bubble determines the compressibility and pressure of the bubble [37,38], which may alter the mechanism and stress required for a dislocation to bypass it.

In this work, we employ MD simulations to investigate the interactions between an edge dislocation and He bubbles. Cu is used here as a model FCC material. With the increase in the He/V ratio, we show that the dislocation-bubble interaction mode changes from dislocation bubble cutting to dislocation climb at room temperature for a large enough bubble. More remarkably, we find that when the ratio of bubble spacing to bubble diameter decreases below a critical value, an alternative, energetically favorable mechanism emerges, in which the entire extended edge dislocation moves to another plane without climbing and without jog formation. The mechanism involves a long series of steps, which we refer to as multi-step bypass (MSB). Both dislocation climb and MSB at room temperature involve vacancy migration from the Cu crystal to the He bubble, resulting in bubble expansion. We show that the conditions for climb and MSB are related to deformation temperature and bubble pressure, and MSB is more energetically favorable compared to the dislocation climb and bubble cutting.

2. Methodology

2.1. Interatomic potential

The interactions among Cu atoms are described by the embedded-atom method (EAM) potential proposed by Mishin et al. [39]. Due to its accurate value for ISFE (44.1 mJ/m^2), this Cu-Cu interaction is widely utilized in the atomistic simulations of dislocation mobility [40,41] and dislocation-obstacle interaction [9,36,42]. For the He-He and He-Cu interactions, we adopted the two-body potential by Kashinath et al. [43]. For this potential, its He-He interaction energy is achieved by integrating the force-distance curve obtained by density functional theory (DFT) calculations. In addition, the defect energies for He defects in Cu by this potential are in excellent agreement with DFT calculations. These potentials have been employed in prior work, involving dislocation-He bubble interactions in Cu [9].
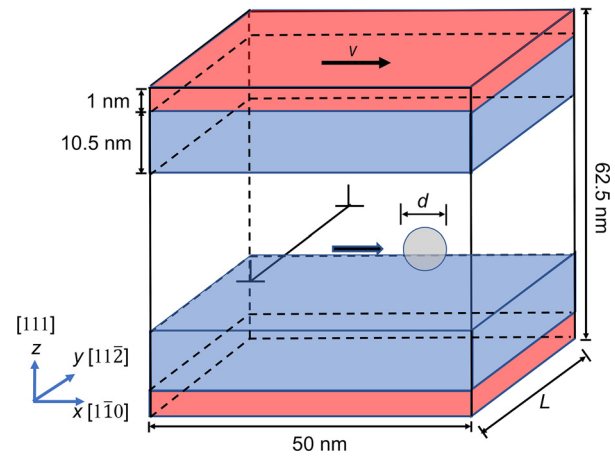
Fig. 1. Schematic of the model set up for the molecular dynamics (MD) simulations. The middle region with no color fill denotes the non-thermostat region, while the red and blue regions are the boundary and thermostat regions, respectively. The symbol '⊥' represents the edge dislocation and on its right side on the glide plane lies the center of the He bubble (or void) with the diameter d. A constant velocity v is imposed in the positive x direction on the top boundary region, while the bottom boundary region is fixed. (For interpretation of the references to colour in this figure legend, the reader is referred to the web version of this article.)

2.2. Molecular dynamics simulation

Our MD simulations were carried out via the Large-scale Atomic/Molecular Massively Parallel Simulator (LAMMPS) [44]. The model configuration for dislocation-bubble/void interaction is displayed in Fig. 1. The single crystal (SC) Cu is oriented with its [1$\bar{1}$0], [11$\bar{2}$] and [111] crystallographic orientations aligned with x-, y- and z-axes, respectively. The x and z dimensions are respectively $\sim$ 50 and $\sim$ 62.5 nm. Their ratio, 0.8, is selected to minimize spurious image stresses that can arise during dislocation-obstacle interaction [42,45]. To investigate its effect, bubble spacing, the y dimension (L), is varied from 10 nm to 20 nm with an increment of 1 nm. We find that $L = 10$ nm represents dense implantation or a high density of He bubbles in the Cu matrix. For a low density of He bubbles, $L = 20$ nm is chosen, since larger L produces similar results to that for $L = 20$ nm.

Periodic boundary conditions (PBCs) are imposed in the x and y directions, while the top and the bottom surfaces with normal in the z direction are maintained as free surfaces. An edge dislocation gliding on the central (111) plane of the simulation cell is inserted into the SC Cu with dislocation line along the y direction and Burgers vector $b = (a_0/2)\langle 110 \rangle$ (a_0 is the lattice parameter). This full edge dislocation dissociates into two $(a_0/6)\langle 112 \rangle$ partial dislocations after energy minimization via the conjugate gradient algorithm. Next, a He bubble is introduced with its center located on the dislocation glide plane and about 20 nm from the right side of the edge dislocation. The diameter of the He bubble is varied over $d = 1, 2, 4, 6$ nm. The most commonly occurring bubble size is $d \leq 6$ nm in the implantation experiments of Cu [5,9].

To construct the He bubble, we first built a void of the same size and then randomly substituted vacancies in the void with He atoms, according to the corresponding He/V ratio R. In this study, the He/V ratio R ranges from $R = 0$, corresponding to a void, to 1.6 using increments of 0.1. The range of He/V ratios $R \leq 2$ is selected based on theoretical calculations [46] and the experiments [47]. Based on our calculations, R larger than 1.6 produces an unstable He bubble in the Cu matrix at 300 K, from which SFs or dislocations punch out from the bubble surface [27]. The bisection method is used to determine the critical temperature T at a given R for either dislocation climb or MSB within an error of ± 0.5 K.

Before shear loading, the thermostat relaxation was conducted at the target temperatures (mainly at 300 K), with the NPT ensemble applied. For the NPT ensemble, the boundary condition (BC) along the z direction is changed to PBC by adding vacuum regions above the top surface and below the bottom surface. This setting is removed when thermostat is completed. More details can be found in Ref. [42]. During shear loading, the system is divided into three regions: the boundary regions, the thermostat regions and the non-thermostat regions, the first two of which are colored in red and blue in Fig. 1, respectively. For the boundary regions with thickness $\sim$ 1 nm, flexible BCs [48] are utilized, where the average atomic velocities in these regions are first calculated and additional velocities are added to ensure that the final velocities of the top and bottom boundary regions reach a constant velocity v and zero, respectively. The value of v is carefully calculated so that a strain rate of 10^7 s^{-1} is achieved. The thermostat regions with NVT ensemble and the thickness of $\sim$ 10.5 nm are implemented above and below the dislocation core to control the simulation temperature and avoid the influence of artificial friction on dislocation dynamics resulting from direct thermostat on dislocation. Finally, the NVE ensemble is utilized in the non-thermostat region to update the atomic positions and velocities. Such a region division have been found in several previous studies [42,49,50].

All visualizations are performed by OVITO [51]. To visualize the dislocation, we use the polyhedral template matching method [52]. In addition, the dislocation lines are recognized by the dislocation analysis (DXA) method [53] and various colors indicate different dislocation types. The Burgers vectors of dislocations are denoted using Thompson's notation shown in Fig. A.1 of the Appendix.

2.3. Volume measurement and visualization of He bubble

The volume of He bubble is measured by the algorithm called construct surface mesh [54] implemented in OVITO. The probe sphere radius and the smoothing level are set to 2 and 1, respectively. The variation of the He bubble in volume is recorded by calculating the ratio of the variation in the current volume to the initial volume. The He bubbles are visualized using the defect mesh in this algorithm.

3. Results

3.1. Shear stress-strain curves

The two important characteristics of a He bubble are its size and He atomic density. The former is measured by the bubble diameter d, while the latter is quantified by He/V ratio R, the number ratio of the He atoms in the bubble to the vacancies in the same bubble. In addition, the bubble spacing L between neighboring bubbles along the dislocation line also affects the critical stress for the dislocation to bypass the bubbles [31]. The L is measured by the distance between the bubble centers. Due to PBCs, L is equal to the y dimension of the atomic model, as shown in Fig. 1. To investigate the effects of He/V ratio R and the ratio of the bubble spacing L to the bubble diameter d, we consider, in our calculations, combinations of $R = 0, 0.5, 1.0, 1.5$, $L = 10, 20$ nm and $d = 1, 2, 4, 6$ nm. For reference, the typical range of bubble diameters in experiments is $d \leq 6$ nm [5,9] and in prior MD simulations, the bubble diameter was fixed to 5 nm [9].

We find in simulation that for the cases involving $d = 1, 2, 4$ nm at 300 K, the edge dislocation cuts through the bubble directly. This outcome follows conventional expectations and is similar to the result in Ding et al.'s work [9]. However, when d further increases to 6 nm, the bypass mechanism depends on the He/V ratio R and any changes in the mechanism can affect the deformation response. Fig. 2(a-b) show the shear stress-strain curves asso-

ciated with the dislocation-bubble interactions for $d = 6$ nm and $R = 0, 0.5, 1.0$ and 1.5 at 300 K. Here, the bubble with $R = 0$ corresponds to the void. In all curves, the stress is initially low and non-negative, being close zero, suggesting the stress to move the dislocation initially is minimal. The position of the dislocation is still far from the bubble. As the dislocation moves close enough to the bubble, the dislocation becomes attracted to the bubble and the dislocation accelerates. This is indicated by a slight stress drop to a negative value. A similar drop in shear stress due to dislocation/bubble attraction is commonly seen in the interactions between dislocation and bubble [31] or void [27] in Fe. When the dislocation finally meets the bubble, the dislocation becomes pinned by it and the stress rises. To force the dislocation to bypass the bubble, the stress needs to increase to a critical value, which corresponds to the peak stress in the stress-strain curve in Fig. 2(a-b).

3.2. Dislocation climb at room temperature

For a large void/bubble spacing ($L = 20$ nm in Fig. 2(c)), the peak stress during the interaction rises slightly from 233 to 238 MPa as R increases from 0 to 1.5. Larger R renders a minor enhancement on the critical bypass stress. When $R = 0, 0.5$ and 1.0, the edge dislocation cuts the bubble, staying on the same glide plane during the process. In contrast, when $R = 1.5$, a portion of dislocation line intersecting the bubble climbs downward and forms a superjog pair in the process, before breaking away from the bubble. The details of the climb process and the related dislocation reactions in the case of $d = 6$ nm, $R = 1.5$ and $L = 20$ nm are provided in Fig. 3. To distinguish the Burgers vector of each partial dislocation, we adopt the conventional classification indicated by Thompson's notations [55] (See Fig. A.1 in the Appendix).

Initially, the perfect dislocation (BA) has dissociated into two partials (δA and Bδ) in Fig. 3(a). As the crystal is sheared, the dislocation glides on the (111) plane toward the bubble and becomes pinned. The two partials reorient their line directions, changing their character, and then constrict to a full screw dislocation. Reorientation of the dislocation line near a free surface can also be found in the experiments and explained by elasticity theory [56,57]. This full screw dislocation then cross slips onto the (11$\bar{1}$) plane and dissociates into two new Shockley partials (γA and Bγ) (See Fig. 3(b)).

Next, a new Hirth dislocation $\gamma\delta$/BA forms, connecting δA, Bδ, γA and Bγ by the reactions of B$\delta = \gamma$A$+\gamma\delta$/BA and δA$+\gamma\delta$/BA $=$ Bγ (Fig. 3(c)). To depin from the bubble, γA and Bγ constrict and further cross slip into δA and Bδ on a lower (111) plane with δA and Bδ connected by another Hirth dislocation $\delta\gamma$/BA. The corresponding dislocation reactions are γA $=$ B$\delta + \delta\gamma$/BA and B$\gamma + \delta\gamma$/BA $=$ δA (Fig. 3(d)).

In contrast, the former Hirth dislocation $\gamma\delta$/BA (7 Å in length) constricts into a point, possibly due to thermal vibration and a superjog is formed between the original (111) plane and a lower (111) plane. Similar to what happens in Fig. 3(b), δA and Bδ on the original (111) plane are recombined into a full screw dislocation BA on the other side of the bubble. Subsequent shear loading causes the full dislocation BA to dissociate into Bγ and γA (Fig. 3(e)). Then, γA further dissociates into Lomer-Cottrell dislocation $\gamma\delta$ and Shockley partial δA on the lower (111) glide plane. Due to PBCs, the two δA on both sides of the bubble and the same lower (111) glide plane connect each other. Finally, another Lomer-Cottrell dislocation $\delta\gamma$ appears and connects Bδ, δA, Bγ and γA (Fig. 3(f)). The related dislocation reactions for the Lomer-Cottrell dislocation pair $\gamma\delta$ and $\delta\gamma$ are B$\delta = B\gamma + \gamma\delta$, $\gamma\delta + \delta$A $= \gamma$A, B$\gamma = B\delta + \delta\gamma$ and $\delta\gamma + \gamma$A $= \delta$A. This $\delta\gamma$ on the upper (111) plane and its counterpart $\gamma\delta$ on the lower (111) plane constitute a new superjog on the other side of the bubble. With the effect of thermal vibration,
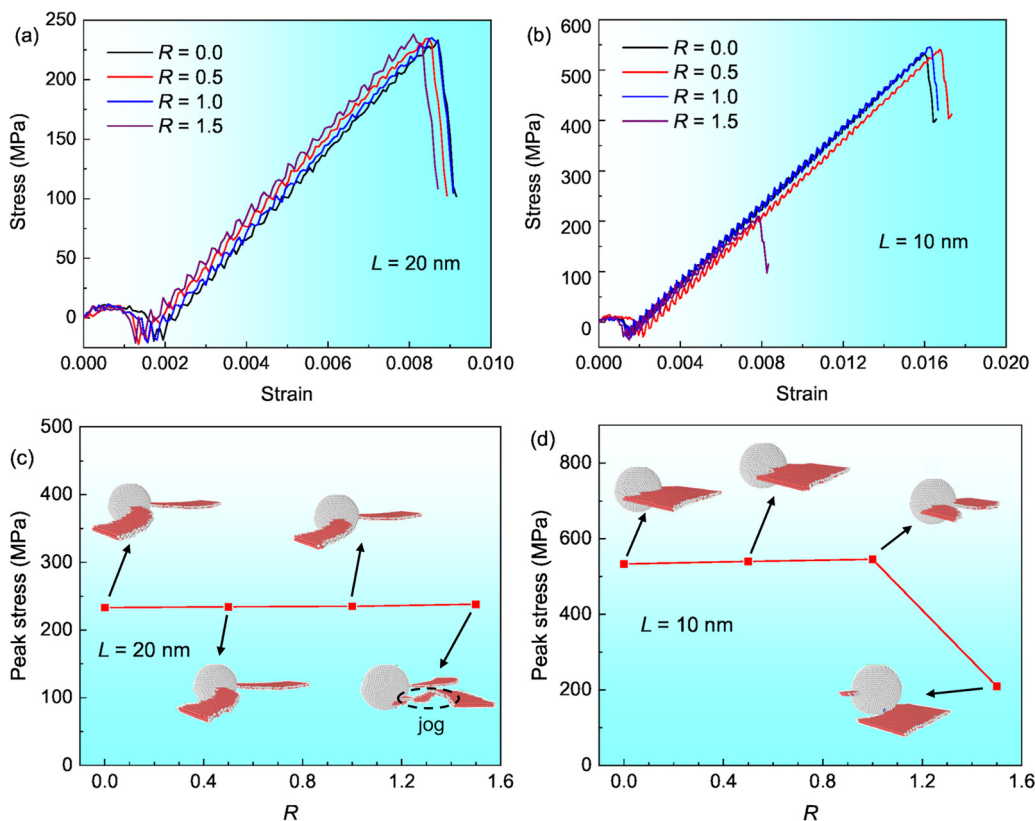
Fig. 2. Shear stress-strain curves of the interactions between an edge dislocation and a He bubble with diameter $d = 6$ nm and different He/V ratios ($R = 0.0$, 0.5, 1.0 and 1.5) at 300 K for bubble spacing (a) $L = 20$ nm and (b) $L = 10$ nm. The peak stress during the interaction as a function of R at 300 K for (c) $L = 20$ nm and (d) $L = 10$ nm. The insets in (c) and (d) denote the corresponding interaction morphology. Note that a He bubble with $R = 0.0$ represents a void.
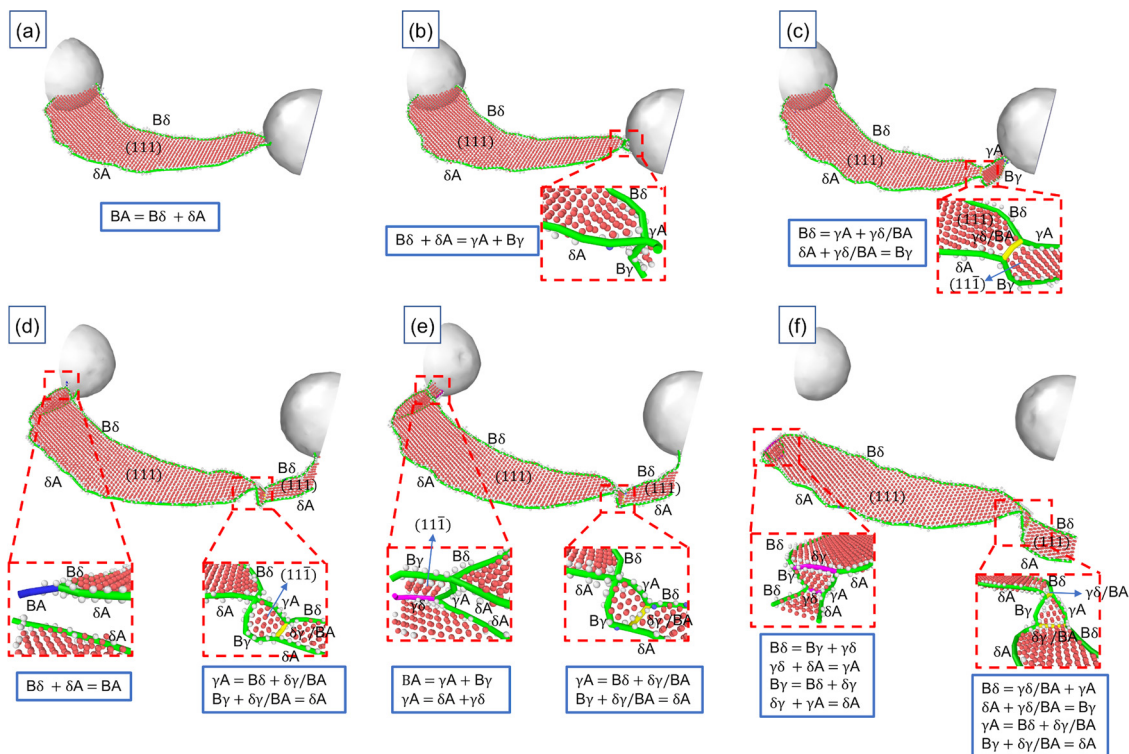
Fig. 3. Snapshots of the climb process for the case with $d = 6$ nm, $R = 1.5$ and $L = 20$ nm at 300 K. The silver sphere represents the He bubble. Face-centered cubic (FCC) atoms belonging to Cu have been removed to better visualize the dislocations. Hexagonal close-packed (HCP) atoms and those with unknown coordination structure are colored red and gray, respectively. Dislocation lines are colored according to dislocation type: Full dislocation, blue; Shockley partial dislocation, green; Lomer-Cottrell dislocation, magenta; and Hirth dislocation, yellow. The names of the Burgers vectors of the dislocations in the FCC system are indicated by the standard Thompson's notation [55]. The related dislocation reactions are shown. The Thompson tetrahedron is also shown in Fig. A.1 in the appendix. (For interpretation of the references to colour in this figure legend, the reader is referred to the web version of this article.)

the constricted point on the other side of the bubble in Fig. 3(e) expands into the Hirth dislocation $\gamma\delta/$BA again in Fig. 3(f).

The climb process is accomplished by first dislocation constriction and second by jog formation, which is the conventional mechanism for climb invoked by a void in BCC Fe [58] or by vacancies in FCC Cu [35]. However, our observation of the climb of an edge dislocation in Cu to overcome a He bubble at room temperature has not been reported before. One previous MD study involved climb of an edge dislocation over a void under high temperatures and using an artificial potential with ultra-high ISFE [36].

3.3. Multi-step bypass at room temperature

Next, we consider dislocation-bubble interactions when the bubble spacing is cut in half, $L = 10$ nm. Fig. 2(d) shows the peak stresses of the stress-strain curves in these cases for $R = 0$, 0.5, 1.0 and 1.5. As expected for $R = 0$, 0.5 and 1.0, the bypass stresses for $L = 10$ nm are much higher than those for $L = 20$ nm. Although for fixed $L = 10$ nm, the enhancement with increasing R is slight, from 533 MPa to 546 MPa. This is characteristic of the cutting mechanism where, just as for $L = 20$ nm, the edge dislocation cuts the bubble on its equatorial plane and then glides away, while remaining on the same glide plane.

When the He/V ratio rises to $R = 1.5$, the expected trend reverses, marked by a steep decline in the peak stress to 209 MPa. Unlike when $L = 20$ nm, raising the He/V ratio in the bubble ($R = 1.5$), did not cause the dislocation to bypass the bubble via climb with jog pair formation. Instead, the entire dislocation line between neighboring bubbles moves from the original plane to a lower parallel plane through a series of steps, each involving either a dissociation or constriction, reactions, and cross slip. Only when it fully transfers to the lower parallel plane does it release itself from the bubble (Fig. 2(d)). During this process, the dislocation does not maintain its edge character but changes its character constantly. Because it includes a series of steps, while at the same time involves the complete transfer of a full edge dislocation from its habit plane to another parallel plane, we refer to the entire process as multi-step bypass (MSB).

To understand how MSB proceeds during the dislocation-bubble interaction, we analyze the partial dislocation reactions in each step for the case of He/V ratio $R = 1.5$, bubble spacing $L = 10$ nm and bubble diameter $d = 6$ nm in Fig. 4. Before shear loading, the full edge dislocation (BA) has dissociated into its leading and trailing partial dislocations (δA and Bδ) on the (111) plane. The initial character angles of both δA and Bδ are 60°. Upon shear loading, these two partials contact the He bubble and then are successively pinned (Fig. 4(a)). The leading partial dislocation δA further decomposes into another Shockley partial βA on the (1$\bar{1}\bar{1}$) plane and a sessile Lomer-Cottrell dislocation $\delta\beta$ lying at the line of intersection between the two planes (Fig. 4(b)). In this way, non-planar dissociation takes place with the appearance of a Shockley partial dislocation βA on the (1$\bar{1}\bar{1}$) plane.

Following the dissociation of δA, $\delta\beta$ further dissociates into δC on the (111) plane and Cβ on the (1$\bar{1}\bar{1}$) plane (Fig. 4(c)). The δC and Cβ are screw dislocations, while Bδ and βA are mixed dislocations with the same character angle of 60°. When the dissociation of $\delta\beta$ has completed, two intrinsic SFs respectively lie on the (111) and (1$\bar{1}\bar{1}$) planes, containing four partials (i.e., Bδ, δC, Cβ and βA in Fig. 4(d)). Hence, the original full dislocation BA decomposes into two extended full dislocations, i.e., BC on the (111) plane and CA on the (1$\bar{1}\bar{1}$) plane, and both of their character angles are 30°. Under shear loading, the partials Cβ and βA in the extended dislocation CA reorient their dislocation lines on the bubble surface and their character angles transform to 30°. After these two partials both reorient, they constrict to a screw full dislocation CA on the bubble surface (Fig. 4(e)).

Next, the full screw-character dislocation CA cross slips from the (1$\bar{1}\bar{1}$) plane to a new (111) plane, which is parallel to the original plane and tangent to the periphery of the bubble, and then dissociates into two new partials (Cδ and δA in Fig. 4(f)). Here, the character angles of both Cδ and δA are 30°. When cross slip ends, CA becomes an extended full dislocation on the lower (111) plane and its total character angle remains 0°. The arrangement of the two SFs appear to be stuck on two parallel (111) glide planes. With further shear loading, the line directions of Cδ and δA align to the y axis ([11$\bar{2}$] direction). As a result, Cδ transforms into a screw dislocation and another partial dislocation δA breaks away from the bubble with its character angle increasing from 30° to 60° (Fig. 4(g)).

As the shear loading continues, the partials Bδ and δC on the upper (111) plane also reorient their line directions on the surface of the bubble, such that when they constrict, they form a full screw dislocation BC (Fig. 4(h)). The reorientation involves a reduction in the character angle from 30° to 0°, similar to the reorientation of the full dislocation CA in Fig. 4(e). Subsequently, dislocation BC cross slips and dissociates into two partials (αC and Bα) on the (1$\bar{1}$1) plane (Fig. 4(i)). As shown in Fig. 4(j), this extended dislocation BC glides down on the (1$\bar{1}$1) plane, as an extended dislocation with two bounding Shockley partials Bα and αC of mixed character 30°.

In the next Fig. 4(k), the leading partial Bα on the (1$\bar{1}$1) plane meets the trailing partial Cδ on the lower (111) plane, reacting to produce a Hirth dislocation $\alpha\delta/$CB. Finally, the trailing partial αC on the (1$\bar{1}$1) plane continues to move and it reacts with $\alpha\delta/$CB, producing a new Shockley partial Bδ with the character angle of 60°. Taken together, we observe that the dissociated edge dislocation BA transitions from one (111) glide plane to another (111) plane 13 atomic planes below it by a series of dislocation dissociations, constrictions, cross slips and reactions. None of the steps involve conventional climb.

3.4. Volume variation of He bubble

To gain insight into the role of He/V ratio in FCC Cu, we first investigate what happens to the bubble in MSB versus the other bypass mechanisms, climb and dislocation cutting. Fig. 5(a) and (c), plots the bubble volume and pressure during its interaction with the dislocation, from first impingement to complete bypass for $L = 20$ nm. When $R = 1.0$, the edge dislocation cuts through the bubble, and when $R = 1.5$, it climbs down. In cutting, the bubble volume and pressure are preserved; however when the dislocation climbs downward, the bubble volume increases and pressure decreases. Two volume changes occur when superjogs have formed during climb, as marked in Fig. 3(b–c) and (d–f), both of which are small, 0.4% and 0.4%. The number of vacancies $n_V = 29$, for each volume change of bubble.

Next, we track the volume and pressure of the bubble in Fig. 5(b) and (d) when the bubble spacing is fine enough, $L = 10$ nm, to potentially cause MSB. When $R = 1.5$ and MSB occurs, first bubble expansion starts at the moment the dislocations Cβ and βA (in Fig. 4(d)), and thus the full dislocation CA reorient to the screw orientation. The bubble enlarges abruptly as the dislocation cross slips downward to another (111) plane, several atomic planes below than the original (111) plane. Similarly, the second volume expansion occurs when Bδ and δC in Fig. 4(h) constrict, and the full dislocation BC reorient to screw and then cross slips. The total change in bubble volume is ~ 4%. The accompanying pressure drop about 14%, suggesting that one reason MSB would be favored over cutting is bubble pressure reduction.

For either dislocation climb or MSB in FCC Cu, the dislocations move downward during their interactions with the bubbles with high He/V ratio and thus high pressure. This is consistent with Os-
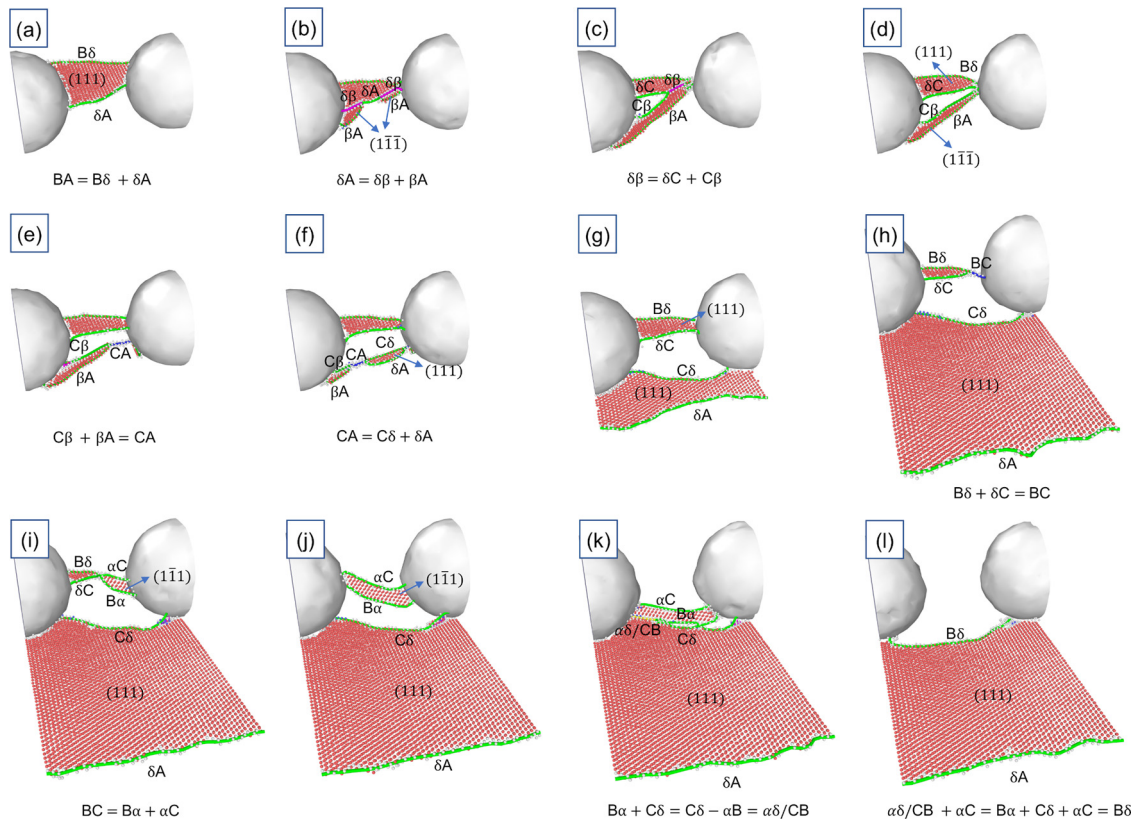
Fig. 4. Snapshots of the multi-step bypass (MSB) process for the case with $d = 6$ nm, $R = 1.5$ and $L = 10$ nm at 300 K. The visualization scheme is the same as that of Fig. 3.
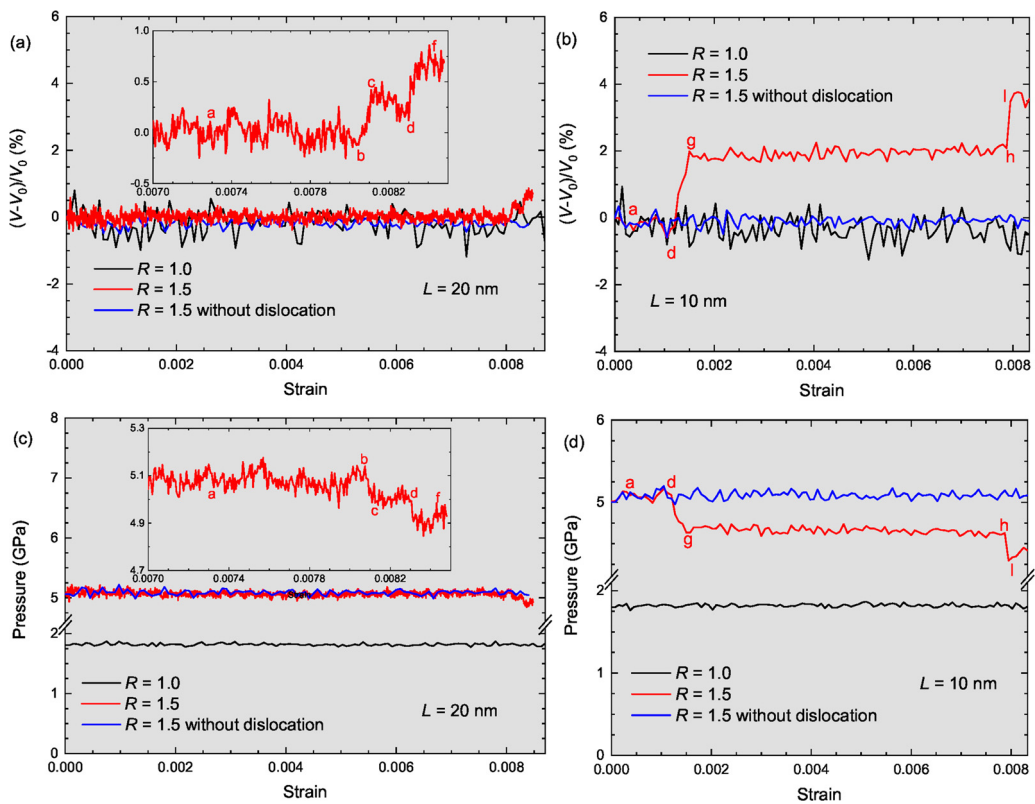

Fig. 5. (a–b) The ratio of the volume variation of He bubble to its initial volume and (c–d) the bubble pressure as a function of strain at 300 K for $L = 20$ nm and $L = 10$ nm with the initial bubble diameter $d = 6$ nm. Three cases are shown. The first two correspond to dislocation-bubble interactions with $R = 1.0$ and 1.5, and the last one, for reference, is deformation of the single-crystal Cu with a bubble of $R = 1.5$, but without the dislocation. The lowercase letters in (a)–(d) correspond to those in the snapshots in Fig. 3 and Fig. 4.
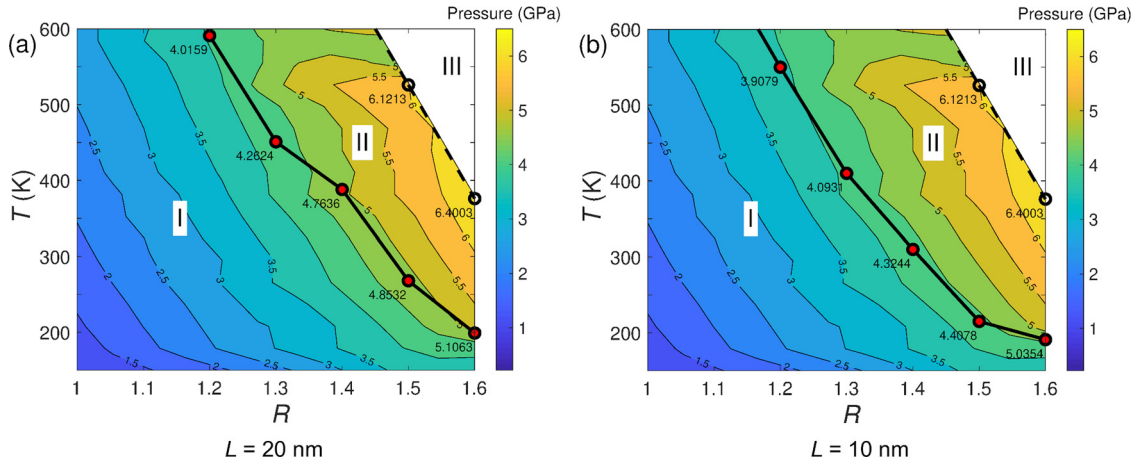
Fig. 6. The pressure of the He bubble ($d = 6$ nm) as the function of temperature T and He/V ratio R for bubble spacing (a) $L = 20$ nm and (b) $L = 10$ nm. The pressure contour is divided into three parts: I, II and III, which are bounded by solid and dashed lines. Regions I, II and III represent the combinations of R and T for bubble-cutting bypass, dislocation climb or MSB, and unstable He bubble, respectively. The red points are the critical combinations of R and T for dislocation climb or MSB, and the numbers around them denote the related gas pressures. (For interpretation of the references to colour in this figure legend, the reader is referred to the web version of this article.)

etsky and Stoller's work [31], where the dislocation climb direction depends on the bubble pressure during dislocation-bubble interaction in BCC Fe. In their work, low bubble pressure promotes an upward dislocation climb, while high bubble pressure aids in a downward climb.

3.5. Conditions for climb and multi-step bypass

As shown in Fig. 5, the bubble tends to increase its volume and thus decrease its pressure by dislocation climb or MSB. In this way, the equilibrium pressure after dislocation-bubble interaction can be reached again. To further reveal the relation between the initial bubble pressure before dislocation-bubble interaction and their interaction mechanism, we carried out calculations for a range of T and R but the same $d = 6$ nm to identify the critical temperature and thus the critical pressure above which climb, in the case of $L = 20$ nm, or MSB, in the case of $L = 10$ nm, occurs. Here, R ranges from 1.0 to 1.6 in increments of 0.1 and the critical temperature T was determined by the bisection method within ± 0.5 K.

Fig. 6 maps the bubble pressure on R and T axes and for $L = 20$ nm, the regime in which cutting (region I), climb (region II), and bubble breakdown (region III) occur. In region III, when the R and T become too great, SFs and dislocations punch out from the He bubble surface, as seen previously [27]. For a void, $R = 0$, no temperature was found to cause climb. The pressure line marking the boundary between regions I and II is the critical pressure for climb. As R increases, the critical temperature T for climb decreases and the critical pressure associated with the onset of climb becomes higher. Similarly, for $L = 10$ nm, we identify a region in the R and T map, at which the pressures are sufficient for MSB. As R increases, the critical temperature to traverse from region I to region II for MSB decreases, while the corresponding pressure rises. These critical pressures for MSB, however, are lower than those for climb. Provided that the bubble density is high enough to enable MSB, the combination of R and T is less severe than those needed for climb. The extreme R and T conditions for the bubble to serve as a source for dislocations, region III, is independent of the bubble density and is the same for both $L = 10$ nm and 20 nm.

The critical pressure exhibits a small dependence on the particular combination of R and T. This dependency arises from the influences of R and T on promoting vacancy motion that supports the climb and MSB processes. A rise in temperature promotes the motion of vacancies and a larger number of He atoms in the bub-

ble attracts vacancies due to higher He-vacancy binding energy (0.34209 eV) than Cu-vacancy binding energy (0.14566 eV), see Fig. B.2 for binding energy calculation.

The bypass mechanisms, climb and MSB, both relieve the pressure of the bubble at fixed R and T because they result in an expansion of the bubble. As the dislocation reorients, reacts, and glides to bypass the bubble, vacancies can be emitted and flow to the bubble. The volume of material affected by the moving dislocation when it bypasses the bubble can be estimated by $\Delta V_C = H \times L_c \times L_p$, where H is the distance traversed normal to the original glide plane, L_p, the interplanar spacing in [1$\bar{1}$0], and L_c is the length of the dislocation that undergoes MSB or climb. In climb, L_c is identified from the simulation in each case, and in MSB, L_c is taken as the bubble spacing 10 nm, since the entire length makes the transition. At the same time, from simulation, we can measure the actual volume expansion of the bubble ΔV_M (see methodology), after the dislocation has bypassed it. Fig. 7 compares ΔV_M and ΔV_C for both climb and MSB events for a range of R and T. It indicates that regardless of R and T, ΔV_M and ΔV_C show a nearly one to one agreement. Further, we observe that MSB involves greater volume change and thus bubble pressure relief than climb.

3.6. Activation energy for climb and multi-step bypass

Finally, we determine and compare the characteristic time t_a required for climb and MSB, spanning from the moment of first contact with the obstacle to final break away from the obstacle. From this calculation, we find that despite the greater number of steps and planes traversed in MSB than in climb, t_a in MSB is much shorter for fixed T and R. The activation energy E_a associated with t_a and T can be estimated using transition state theory [59], via $E_a = k_B T \ln \left(\frac{\nu_D b t_a}{2d} \right)$, where k_B, ν_D, and b, are Boltzmanns constant, Debye frequency, and the value of the Burgers vector, respectively. For Cu, $b = a_0 / \sqrt{2} = 0.25562$ nm and $\nu_D = 4.46 \times 10^{13}$ Hz [60]. For the comparison, a critical temperature T_c for climb or MSB was identified for each R, such that at 1 K lower, the dislocation cuts the bubble. In Fig. 8(a), we compare E_a corresponding to the two bypass mechanisms, cutting and climb, when the bubble spacing is $L = 20$ nm, above critical length for MSB. The critical temperatures T_c are provided above the data bars. For fixed R, the activation energy for climb is only slightly smaller than that for bubble-cutting. The results also show that higher R lowers the E_a for both, mak-
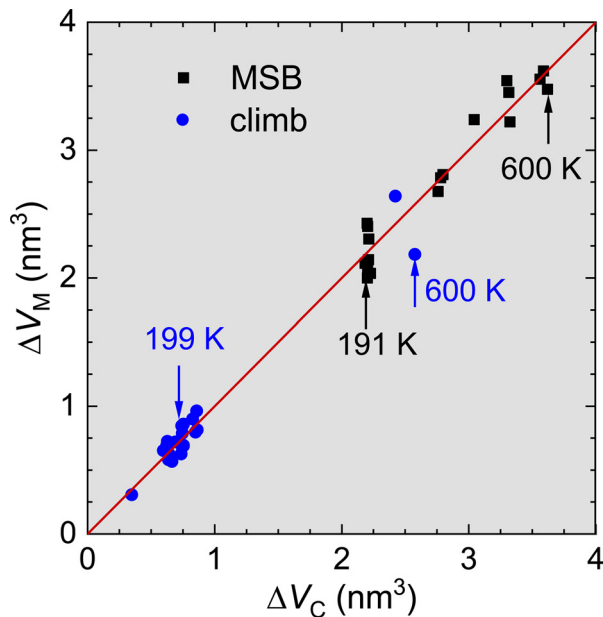
Fig. 7. The measured volume expansion of the He bubble via the algorithm of construct surface mesh [54] implemented in the OVITO [51] as a function of the calculated theoretical value. All the points are extracted from Region II in Fig. 6. The temperature for MSB ranges from 191 K to 600 K, while that for climb from 199 K to 600 K.

ing these bypass mechanisms easier. In the event that MSB is possible, with finer spacing, $L = 10$ nm (Fig. 8(b)), the E_a for MSB is noticeably smaller than that for bubble-cutting at a given R and near or at the threshold T_c. As before, the E_a for MSB decreases with increases in R, indicating greater amounts of He in the bubble promotes MSB over cutting. Overall, when comparing the critical R and T values needed to invoke climb or MSB, we find that MSB is the more favorable mechanism.

4. Discussion

The MSB is a novel bypass mechanism that appears to arise only in the severest of conditions of high bubble density (tight spacing) and high He transmutation/implantation rate (high He/V ratio). Both conditions are representative of those that can occur in metals under high-dose irradiation [9]. The role of fine spacing

in promoting MSB likely arises from one among the many steps in the MSB process—the reorientation of the dislocation line, which is a near free-surface effect from mixed character to screw character. This maneuver is driven by energy minimization near a free surface, as the screw oriented dislocation has the lowest elastic line energy [61,62]. Previous experiments have observed such dislocation rotation from mixed to screw orientation when the dislocation ends on a flat surface of CuAl thin foil [56] and silicon crystal [57]. For the same conditions in which MSB emerged, i.e., $d = 6$ nm and $R = 1.5$ at room temperature, we repeated the calculation for a series of L ranging from 10 nm to 20 nm in increments of 1 nm, finding that the critical bubble spacing below which MSB occurs over climb is $L = 11$ nm. The inner surface-to-surface spacing in the crystal in which the dislocation transfers is only 5 nm. The extent of the "bubble surface effect" depends on several factors, such as the elastic modulus of the material, temperature, and He/V ratio. In the case of $d = 6$ nm, $R = 1.5$ and room temperature, the extent is short, no more than ≈ 2.5 nm from the bubble surface. For larger spacing, much of the bypassing dislocation line lies out of reach and MSB is not possible, forcing the dislocation to climb to circumvent the bubble conventionally. In addition, cross slip on the bubble surface is another important step in the MSB process. Thus, the role of bubble spacing in MSB process may also depend on the dislocation dissociation (e.g. stacking fault energy) and bubble size (e.g., bubble surface curvature).

We find that the other severe condition for MSB is a high He/V ratio in the nanobubbles. This response may be unique to the FCC crystals, like the Cu studied here, in which dislocations are extended and do not climb easily. To date, MSB has not been reported in BCC crystals, regardless of He/V ratio. Edge dislocations in BCC materials are not extended and when interacting with a void or bubble, they will climb. The interesting similarity lies in the direction of bypass. In BCC crystals, for high He/V bubbles, the edge dislocation will climb downwards but for the voids or low He/V bubbles, it climbs upwards. Likewise in FCC crystals, MSB in tight nanobubble spacings or climb in wide spacings involves downward motion when He/V ratios are high. In the case of BCC Fe, the low He/V nanobubble or void acts as a vacancy source, causing the dislocation to climb upwards and the bubble to shrink [17,18,31,33]. In the case of FCC and BCC crystals, the drive for vacancies to bind to He atoms in the bubble is the likely cause for the downward motion of dislocation when the He/V ratio in the bubble becomes sufficiently high [31].
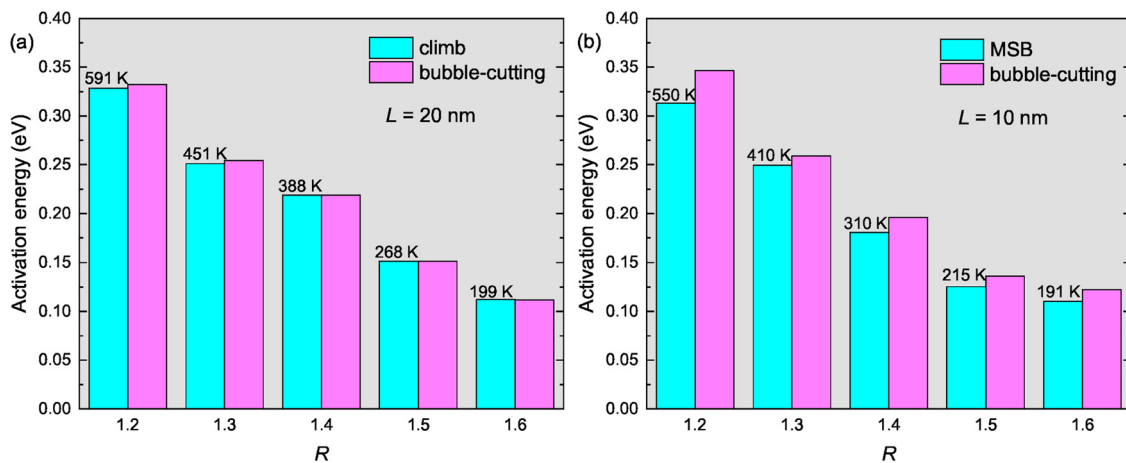
Fig. 8. The activation energy for the critical interaction mechanism as a function of He/V ratio R for (a) $L = 20$ nm and (b) $L = 10$ nm. The values above the blue bars in (a) and (b) denote the critical temperatures required for climb and MSB, respectively. The critical temperature for bubble-cutting mechanism is approximately 1 K lower than those given. Here, all the cases correspond to $d = 6$ nm. (For interpretation of the references to colour in this figure legend, the reader is referred to the web version of this article.)

In addition, the bubble pressure after mechanical equilibrium varies with the He/V ratio, temperature, and bubble size. For given He/V ratio and temperature, the equilibrium pressure decreases with an increasing bubble size. Furthermore, for a given bubble size, the equilibrium pressure increases with temperature and He/V ratio (Fig. 6). Such results are consistent with Stoller and Osetsky's study [38]. Based on their study, it is possible that large bubbles with $d = 6$ nm in our simulations are overpressurized to some extent when the He/V ratio $R \geq 1$.

Depending on the bubble pressure, He bubbles in irradiated metals can serve as hard or soft obstacles, which is possibly related to strengthening or softening in metals. Wang et al. [7] found the implanted He bubbles increase the strength of single-crystal Cu nanopillars but impair their ductility. However, Liu et al. [63] argued that He bubbles can induce softening rather than strengthening in α-Zr, once the bubble size exceeds a threshold. Recent studies report that He-implantation can simultaneously lead to greater strength and better ductility than un-irradiated Cu [9,64], an attribute that breaks the common strength/ductility trade-off [65]. They attributed hardening to the reduced dislocation mean free path and postponement of strain localization by high He bubble densities. Our calculations show that MSB is promoted by large He/V ratio and high temperature, and has a much lower critical bypass stress than conventional bypass mechanisms of climb or bubble cutting at room temperature, suggesting that bubbles with high pressure may be soft obstacles and responsible for material softening.

MSB is studied here as a bypass mechanism for edge-character dislocations. Deformation generally involves the motion of dislocations of all characters. MSB is obviously not possible for screw-oriented dislocations, which can cross slip over obstacles, like nanobubbles. However, a complex bypass mechanism, such as MSB, involving a series of dislocation constrictions, dissociation, cross slip, and reactions may be a possible bypass mechanism for mixed dislocations, depending on the relative size of the screw component. A comprehensive understanding of the mechanical performance of irradiated metals with gas nanobubbles, would include mapping the regime of He/V ratio and nanobubble density at which bypass mechanisms convert from the conventional to complex.

5. Conclusions

In summary, we identify a unique mechanism, called MSB, which an edge dislocation uses to bypass a He bubble in a FCC metal, Cu. MSB emerges as a more favorable mechanism compared to conventional ones in the event the concentration of He in the bubble is sufficiently high, even at room temperature. We show that MSB is also accompanied by a drop in bubble pressure and determine the conditions of He-to-vacancy ratio in the bubble and temperature in which MSB is favored over bubble cutting.

Declaration of Competing Interest

The authors declare that they have no known competing financial interests or personal relationships that could have appeared to influence the work reported in this paper.
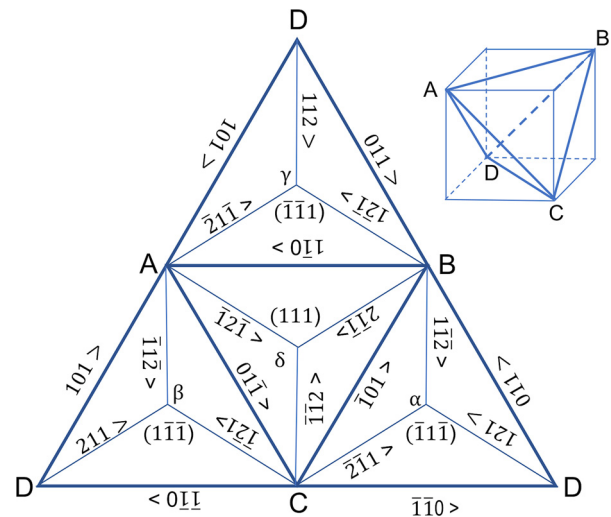
Appendix A. Thompson tetrahedron

Fig. A.1. The Thompson tetrahedron opened up at the corner D. The '>' in the number notation implies the vector direction.

Appendix B. Binding energy calculation

To calculate the binding energy of the vacancy and He or Cu atoms, we built two different SC Cu models with their [100], [010] and [001] crystallographic orientations aligned with x-, y- and z-axes, respectively. The dimensions of these two models are $3.6 \times 3.6 \times 7.2$ nm^3 and $3.6 \times 3.6 \times 3.6$ nm^3, respectively. As shown in Fig. B.2, one Cu atom in the smaller Cu model is removed or substituted by a He atom to create the Cu model containing one vacancy or one He-vacancy cluster, denoted by Model I and II, respectively. Two nonadjacent Cu atoms neighboring to the same Cu atom in the larger Cu model are deleted to generate the Cu model with two separated vacancies bound to the same Cu atom (Model III). To generate Model IV with the cluster containing one He atom and two vacancies, two neighboring atoms of the original larger Cu model are removed and then only one of the vacancies is filled by one He atom. After energy minimization, we obtain the total energies for all four models: E_1, E_2, E_3 and E_4. The binding energy for the vacancy and Cu atom is $E_{CuV} = 2E_1 - E_3 = 0.14566$ eV, while that for the vacancy and He atom is $E_{HeV} = E_1 + E_2 - E_4 = 0.34209$ eV.
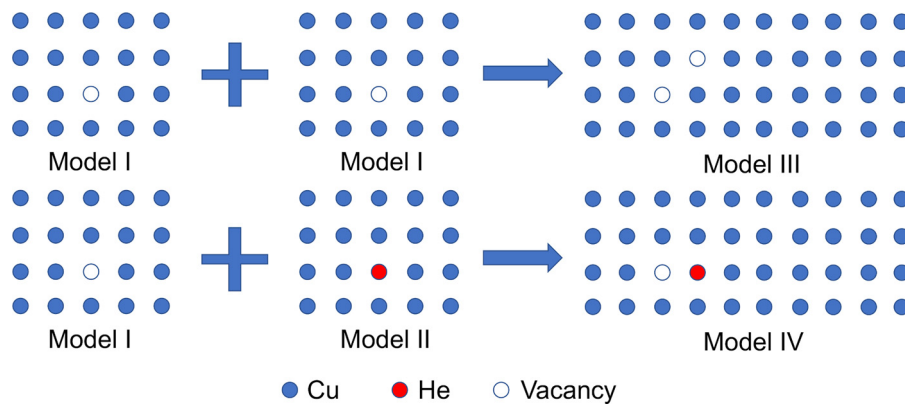
Fig. B.2. Schematic for the calculation of the binding energy of vacancy and Cu/He atoms. The blue, red and unfilled circles represent Cu, He atoms and vacancy in lattice sites, respectively. (For interpretation of the references to colour in this figure legend, the reader is referred to the web version of this article.)

References

[1] S.J. Zinkle, G. Was, Materials challenges in nuclear energy, Acta Mater. 61 (3) (2013) 735–758.

[2] S.-H. Li, J.-T. Li, W.-Z. Han, Radiation-induced helium bubbles in metals, Materials 12 (7) (2019) 1036.

[3] K. Yutani, H. Kishimoto, R. Kasada, A. Kimura, Evaluation of helium effects on swelling behavior of oxide dispersion strengthened ferritic steels under ion irradiation, J. Nucl. Mater. 367 (2007) 423–427.

[4] R. Bès, C. Gaillard, N. Millard-Pinard, S. Gavarini, P. Martin, S. Cardinal, C. Esnouf, A. Malchere, A. Perrat-Mabilon, Xenon behavior in TiN: A coupled XAS/TEM study, J. Nucl. Mater. 434 (1–3) (2013) 56–64.

[5] N. Li, M. Nastasi, A. Misra, Defect structures and hardening mechanisms in high dose helium ion implanted Cu and Cu/Nb multilayer thin films, Int. J. Plast. 32 (2012) 1–16.

[6] Q. Guo, P. Landau, P. Hosemann, Y. Wang, J.R. Greer, Helium implantation effects on the compressive response of Cu nanopillars, Small 9 (5) (2013) 691–696.

[7] Z.-J. Wang, F.I. Allen, Z.-W. Shan, P. Hosemann, Mechanical behavior of copper containing a gas-bubble superlattice, Acta Mater. 121 (2016) 78–84.

[8] T. Yamamoto, G.R. Odette, H. Kishimoto, J.-W. Rensman, P. Miao, On the effects of irradiation and helium on the yield stress changes and hardening and non-hardening embrittlement of ∼8Cr tempered martensitic steels: compilation and analysis of existing data, J. Nucl. Mater. 356 (1–3) (2006) 27–49.

[9] M.-S. Ding, J.-P. Du, L. Wan, S. Ogata, L. Tian, E. Ma, W.-Z. Han, J. Li, Z.-W. Shan, Radiation-induced helium nanobubbles enhance ductility in submicron-sized single-crystalline copper, Nano Lett. 16 (7) (2016) 4118–4124.

[10] A. Reichardt, M. Ionescu, J. Davis, L. Edwards, R. Harrison, P. Hosemann, D. Bhattacharyya, In situ micro tensile testing of He^{+2} ion irradiated and implanted single crystal nickel film, Acta Mater. 100 (2015) 147–154.

[11] M.-S. Ding, L. Tian, W.-Z. Han, J. Li, E. Ma, Z.-W. Shan, Nanobubble fragmentation and bubble-free-channel shear localization in helium-irradiated submicron-sized copper, Phys. Rev. Lett. 117 (21) (2016) 215501.

[12] P. Landau, Q. Guo, P. Hosemann, Y. Wang, J.R. Greer, Deformation of as-fabricated and helium implanted 100 nm-diameter iron nano-pillars, Mater. Sci. Eng. A 612 (2014) 316–325.

[13] W. Yang, Grain boundary segregation in solution-treated Nimonic PE16 during neutron irradiation, J. Nucl. Mater. 108 (1982) 339–346.

[14] R. Wright, C.D. Van Siclen, In-situ TEM observations of helium bubble interactions with dislocations, J. Nucl. Mater. 206 (1) (1993) 87–93.

[15] T. Hatano, H. Matsui, Molecular dynamics investigation of dislocation pinning by a nanovoid in copper, Phys. Rev. B 72 (9) (2005) 094105.

[16] Y. Cheng, E. Bitzek, D. Weygand, P. Gumbsch, Atomistic simulation of dislocation–void interactions under cyclic loading, Modelling Simul. Mater. Sci. Eng. 18 (2) (2010) 025006.

[17] P. Grammatikopoulos, D. Bacon, Y.N. Osetsky, The influence of interaction geometry on the obstacle strength of voids and copper precipitates in iron, Model. Simul. Mater. Sci. Eng. 19 (1) (2010) 015004.

[18] Y.N. Osetsky, D.J. Bacon, Atomic-scale mechanisms of void hardening in bcc and fcc metals, Phil. Mag. 90 (7–8) (2010) 945–961.

[19] A. Dutta, M. Bhattacharya, N. Gayathri, G. Das, P. Barat, The mechanism of climb in dislocation–nanovoid interaction, Acta Mater. 60 (9) (2012) 3789–3798.

[20] K. Asari, O. Hetland, S. Fujita, M. Itakura, T. Okita, The effect of stacking fault energy on interactions between an edge dislocation and a spherical void by molecular dynamics simulations, J. Nucl. Mater. 442 (1–3) (2013) 360–364.

[21] R. Schäublin, S.H. Haghighat, Molecular dynamics study of strengthening by nanometric void and Cr alloying in Fe, J. Nucl. Mater. 442 (1–3) (2013) S643–S648.

[22] M. Bahramyan, R.T. Mousavian, D. Brabazon, Molecular dynamic simulation of edge dislocation-void interaction in pure Al and Al-Mg alloy, Mater. Sci. Eng. A 674 (2016) 82–90.

[23] B. Zhu, M. Huang, Z. Li, Atomic level simulations of interaction between edge dislocations and irradiation induced ellipsoidal voids in alpha-iron, Nucl. Instrum. Methods B 397 (2017) 51–61.

[24] J. Byggmästar, F. Granberg, K. Nordlund, Molecular dynamics simulations of thermally activated edge dislocation unpinning from voids in α-Fe, Phys. Rev. Mater. 1 (5) (2017) 053603.

[25] S. Xu, D.L. McDowell, I.J. Beyerlein, Sequential obstacle interactions with dislocations in a planar array, Acta Mater. 174 (2019) 160–172.

[26] S.H. Haghighat, R. Schaeublin, Molecular dynamics modeling of cavity strengthening in irradiated iron, J. Comp. Aided Mater. Des. 14 (1) (2007) 191.

[27] R. Schäublin, Y. Chiu, Effect of helium on irradiation-induced hardening of iron: A simulation point of view, J. Nucl. Mater. 362 (2–3) (2007) 152–160.

[28] R. Schäublin, N. Baluc, Radiation damage in ferritic/martensitic steels for fusion reactors: a simulation point of view, Nucl. Fusion 47 (12) (2007) 1690.

[29] S. Hafez Haghighat, R. Schäublin, Influence of the stress field due to pressurized nanometric He bubbles on the mobility of an edge dislocation in iron, Phil. Mag. 90 (7–8) (2010) 1075–1100.

[30] L. Yang, Z.Q. Zhu, S. Peng, X. Long, X. Zhou, X. Zu, H.L. Heinisch, R.J. Kurtz, F. Gao, Effects of temperature on the interactions of helium–vacancy clusters with gliding edge dislocations in α-Fe, J. Nucl. Mater. 441 (1–3) (2013) 6–14.

[31] Y.N. Osetsky, R.E. Stoller, Atomic-scale mechanisms of helium bubble hardening in iron, J. Nucl. Mater. 465 (2015) 448–454.

[32] Y. Abe, T. Tsuru, S. Shi, N. Oono, S. Ukai, Effect of the dilation caused by helium bubbles on edge dislocation motion in α-iron: molecular dynamics simulation,, J. Nucl. Sci. Technol. 53 (10) (2016) 1528–1534.

[33] Y.N. Osetsky, D.J. Bacon, Void and precipitate strengthening in α-iron: what can we learn from atomic-level modelling? J. Nucl. Mater. 323 (2–3) (2003) 268–280.

[34] P.M. Anderson, J.P. Hirth, J. Lothe, Theory of dislocations, Cambridge University Press, 2017.

[35] A. Abu-Odeh, M. Cottura, M. Asta, Insights into dislocation climb efficiency in FCC metals from atomistic simulations, Acta Mater. 193 (2020) 1–10.

[36] K. Doihara, T. Okita, M. Itakura, M. Aichi, K. Suzuki, Atomic simulations to evaluate effects of stacking fault energy on interactions between edge dislocation and spherical void in face-centred cubic metals, Phil. Mag. 98 (22) (2018) 2061–2076.

[37] A. Caro, J. Hetherly, A. Stukowski, M. Caro, E. Martinez, S. Srivilliputhur, L. Zepeda-Ruiz, M. Nastasi, Properties of helium bubbles in Fe and FeCr alloys, J. Nucl. Mater. 418 (1–3) (2011) 261–268.

[38] R. Stoller, Y.N. Osetsky, An atomistic assessment of helium behavior in iron, J. Nucl. Mater. 455 (1–3) (2014) 258–262.

[39] Y. Mishin, M. Mehl, D. Papaconstantopoulos, A. Voter, J. Kress, Structural stability and lattice defects in copper: *abinitio*, tight-binding, and embedded-atom calculations, Phys. Rev. B 63 (22) (2001) 224106.

[40] H. Tsuzuki, P.S. Branicio, J.P. Rino, Molecular dynamics simulation of fast dislocations in copper, Acta Mater. 57 (6) (2009) 1843–1855.

[41] Q.-J. Li, J. Li, Z.-W. Shan, E. Ma, Strongly correlated breeding of high-speed dislocations, Acta Mater. 119 (2016) 229–241.

[42] W.-R. Jian, M. Zhang, S. Xu, I.J. Beyerlein, Atomistic simulations of dynamics of an edge dislocation and its interaction with a void in copper: a comparative study, Model. Simul. Mater. Sci. Eng. 28 (4) (2020) 045004.

[43] A. Kashinath, M.J. Demkowicz, A predictive interatomic potential for He in Cu and Nb, Model. Simul. Mater. Sci. Eng. 19 (3) (2011) 035007.

[44] S. Plimpton, Fast parallel algorithms for short-range molecular dynamics, J. Comp. Phys. 117 (1) (1995) 1–19.

[45] B. Szajewski, W. Curtin, Analysis of spurious image forces in atomistic simulations of dislocations, Model. Simul. Mater. Sci. Eng. 23 (2) (2015) 025008.

[46] S. Valone, M. Baskes, R. Martin, Atomistic model of helium bubbles in gallium-stabilized plutonium alloys, Phys. Rev. B 73 (21) (2006) 214209.

[47] A. Schwartz, M. Wall, T. Zocco, W. Wolfer, Characterization and modelling of helium bubbles in self-irradiated plutonium alloys, Phil. Mag. 85 (4–7) (2005) 479–488.

[48] D. Rodney, Activation enthalpy for kink-pair nucleation on dislocations: Comparison between static and dynamic atomic-scale simulations, Phys. Rev. B 76 (14) (2007) 144108.

[49] J. Cho, J.-F. Molinari, G. Anciaux, Mobility law of dislocations with several character angles and temperatures in FCC aluminum, Int. J. Plast. 90 (2017) 66–75.

[50] K. Dang, D. Bamney, K. Bootsita, L. Capolungo, D.E. Spearot, Mobility of dislocations in Aluminum: Faceting and asymmetry during nanoscale dislocation shear loop expansion, Acta Mater. 168 (2019) 426–435.

[51] A. Stukowski, Visualization and analysis of atomistic simulation data with OVITO–the Open Visualization Tool, Model. Simul. Mater. Sci. Eng. 18 (1) (2009) 015012.

[52] P.M. Larsen, S. Schmidt, J. Schiøtz, Robust structural identification via polyhedral template matching, Modelling Simul. Mater. Sci. Eng. 24 (5) (2016) 055007.

[53] A. Stukowski, V.V. Bulatov, A. Arsenlis, Automated identification and indexing of dislocations in crystal interfaces, Model. Simul. Mater. Sci. Eng. 20 (8) (2012) 085007.

[54] A. Stukowski, Computational analysis methods in atomistic modeling of crystals, JOM 66 (3) (2014) 399–407.

[55] N. Thompson, Dislocation nodes in face-centred cubic lattices, Proc. Phys. Soc. B 66 (6) (1953) 481.

[56] P. Hazzledine, H.-P. Karnthaler, E. Wintner, Non-parallel dissociation of dislocations in thin foils, Phil. Mag. 32 (1) (1975) 81–97.

[57] A. George, G. Champier, On the cross-slip of isolated dislocations at the surface of silicon crystals, Scr. Metall. 14 (4) (1980) 399–403.

[58] Y.N. Osetsky, D. Bacon, V. Mohles, Atomic modelling of strengthening mechanisms due to voids and copper precipitates in α-iron,, Phil. Mag. 83 (31–34) (2003) 3623–3641.

[59] G. Monnet, Y.N. Osetsky, D.J. Bacon, Mesoscale thermodynamic analysis of atomic-scale dislocation–obstacle interactions simulated by molecular dynamics, Phil. Mag. 90 (7–8) (2010) 1001–1018.

[60] A.V. Evteev, L. Momenzadeh, E.V. Levchenko, I.V. Belova, G.E. Murch, Molecular dynamics prediction of phonon-mediated thermal conductivity of f.c.c. Cu, Philos. Mag. 94 (7) (2014) 731–751.

[61] R. Gevers, S. Amelinckx, P. Delavignette, A surface effect associated with dislocation ribbons, Phil. Mag. 6 (72) (1961) 1515–1526.

[62] S. Shaibani, P. Hazzledine, The displacement and stress fields of a general dislocation close to a free surface of an isotropic solid, Phil. Mag. A 44 (3) (1981) 657–665.

[63] S.-M. Liu, S.-H. Li, W.-Z. Han, Effect of ordered helium bubbles on deformation and fracture behavior of α-Zr, J. Mater. Sci. Technol. 35 (7) (2019) 1466–1472.

[64] S.-H. Li, J. Zhang, W.-Z. Han, Helium bubbles enhance strength and ductility in small-volume Al-4Cu alloys, Scr. Mater. 165 (2019) 112–116.

[65] I. Ovid'Ko, R. Valiev, Y. Zhu, Review on superior strength and enhanced ductility of metallic nanomaterials, Prog. Mater. Sci. 94 (2018) 462–540.